


The dynamics of coherent modes of gradient drift instabilities in a small magnetron discharge plasma

Cite as: J. Appl. Phys. **127**, 223301 (2020); <https://doi.org/10.1063/5.0006320>

Submitted: 01 March 2020 . Accepted: 22 May 2020 . Published Online: 08 June 2020

A. Marcovati , T. Ito , and M. A. Cappelli 

COLLECTIONS

 This paper was selected as Featured



View Online



Export Citation



CrossMark

ARTICLES YOU MAY BE INTERESTED IN

[Synthesis, properties, and applications of 2D amorphous inorganic materials](#)

Journal of Applied Physics **127**, 220901 (2020); <https://doi.org/10.1063/1.5144626>

[Domain walls in antiferromagnets: The effect of Dzyaloshinskii–Moriya interactions](#)

Journal of Applied Physics **127**, 223908 (2020); <https://doi.org/10.1063/5.0009409>

[Trielectrode plasma reactor for water treatment](#)

Journal of Applied Physics **127**, 223303 (2020); <https://doi.org/10.1063/5.0005197>

Lock-in Amplifiers
up to 600 MHz



The dynamics of coherent modes of gradient drift instabilities in a small magnetron discharge plasma

Cite as: J. Appl. Phys. **127**, 223301 (2020); doi: [10.1063/5.0006320](https://doi.org/10.1063/5.0006320)
Submitted: 1 March 2020 · Accepted: 22 May 2020 ·
Published Online: 8 June 2020



A. Marcovati,¹  T. Ito,^{1,2,a)}  and M. A. Cappelli^{1,b)} 

AFFILIATIONS

¹High Temperature Gasdynamics Laboratory, Stanford University, Stanford, California 94305, USA

²Center for Atomic and Molecular Technologies, Graduate School of Engineering, Osaka University, 2-1 Yamadaoka, Suita, Osaka 565-0871, Japan

^{a)}**Affiliation when this research was conducted. Now at:** Graduate School of Frontier Sciences, The University of Tokyo, Tokyo, Japan.

^{b)}**Electronic mail:** cap@stanford.edu

ABSTRACT

We report on the dynamic behavior of gradient-driven drift waves in a strongly obstructed magnetron discharge. The magnetron has a magnetic topology that results in a toroidal plasma within the gap and supports the development of very coherent modes of rotating plasma structures. The modes and their rotation are present over a wide range of conditions, and the rotation is retrograde to the usual externally imposed $E \times B$ direction. This feature seems to be unique to this device and is attributed to a field reversal due to the strong anode-directed electron diffusion that arises from large axial plasma density gradients. A multi-fluid model is proposed, and a Fourier analysis of the linearized equations results in the identification of conditions that support the growth of these instabilities and their transitions across mode symmetries, controlled experimentally by varying the discharge voltage. The model also provides insight on the possible mechanism driving cross-field particle transport. Experiments are carried out with a segmented anode to confirm the localized current flow concomitant with the presence of a coherent structure. These segment currents together with high speed videography unambiguously confirm the direction of plasma rotation and reveal the existence of a stochastic regime between voltage-controlled mode transitions. An analysis of the segment currents in this regime indicates that the lower frequency state decays into a spectrum of coherent higher frequency states that exhibit features consistent with a three-wave nonlinear parametric mixing process.

Published under license by AIP Publishing. <https://doi.org/10.1063/5.0006320>

I. INTRODUCTION

Magnetron and Penning discharge configurations form plasmas in the regions of perpendicular electric and magnetic ($E \times B$) fields. Renewed interest in the study of such discharges is due in part to material deposition methods that involve high power impulse magnetron sputtering (HPIMS)¹ and to Hall effect thrusters² used in space propulsion to control geosynchronous satellites and future lower earth orbit constellations.³ In most practical devices, spatial gradients exist in the plasma properties driven by kinetic, electrostatic, and magnetostatic pressure. The gradients in confined plasmas provide an inevitable source of instability, hence the name “universal instabilities.”⁴ Drift-wave instabilities in magnetron discharges,

driven by gradients in density and magnetic field, are a subset of these universal instabilities under conditions of magnetic field confinement.⁵

The first analytical description of drift-wave instabilities in a partially ionized, collisional, and fully magnetized plasma is generally attributed to Simon and Hoh.^{6,7} The mechanism that drives the Simon–Hoh instability (SHI) is the formation of an electric field that is orthogonal to the external $E \times B$ direction due to the disparity in electron and ion drift velocities. This is because the ion drift velocity is reduced relative to that of the electrons by the higher ion-neutral friction. However, most laboratory and commercial plasmas are only partially magnetized; i.e., the electrons are magnetized and confined with a gyroradius that is smaller than the

characteristic scale of the discharge ($\rho_e \ll L_c$), whereas the ions, being much heavier, have a large gyroradius ($\rho_i \gg L_c$) and escape the plasma region in the direction of the electric field. The SHI mechanism was modified for the case of non-magnetized ions and a collisionless plasma⁸ although with the disparity in magnetization of ions and electrons (and not friction) as the cause for the formation of the out of plane ($E \times B$ -directed) electrostatic field. In both the SHI and the modified-SHI (MSHI), the necessary condition for the formation of the instability, in the presence of a uniform magnetic field, is that the applied electric field must be in the same direction of the density gradient ($\nabla n_e \cdot E_0 > 0$). Evidence that the instability is related to the disparate confinement of electrons and ions is the observation that the frequency of instabilities is of the order of the inverse of the transient-time of the ions in the plasma region as they are accelerated outward.

Drift-wave instabilities in some $E \times B$ discharges exhibit spatial and temporal coherence characteristics of self-organization.^{9–12} This self-organization, rendered unstable by gradients in the plasma density or the magnetic field as discussed above, appears to be further destabilized by the diffusion of plasma along the magnetic field.¹³ For example, we have reported strong coherence and self-organization in a direct current (DC) magnetron microdischarge.^{14,15} From high speed videography of the plasma emission, the observed structures appear to propagate in the $-E \times B$ direction, opposite to what has been generally reported in HiPIMS sources,^{16–18} although in some circumstances,¹⁹ the coherent structures in HiPIMS also appear to reverse in their direction.

In a recent paper,²⁰ we showed that the azimuthally propagating coherent structures in our small magnetron also undergo distinct mode transitions, with higher order modes favored at a lower discharge voltage. In that study, we presented the results of a gradient-driven drift-wave model similar to that developed to understand low frequency disturbances seen in Hall thrusters.^{21,22} The model included plasma diffusion along the magnetic field, expanding the domain of instability. We showed that the model can account for the dispersion seen in our experiments but presumes that a field reversal is present within the gap, due to the necessity to restrict an anode-directed electron flux associated with the high plasma density gradients. Field reversals are commonly seen in simulations of Hall thrusters^{23,24} and have been proposed to explain transient behavior²⁵ and enhanced ion back-flow²⁶ in HiPIMS sources.

In this paper, we describe the theory in detail and formulate perturbations of the fluid equations to factor out non-linear terms for future numerical simulations. Through linearization and a Fourier analysis, we derive the dispersion relations and show that the transitions between modes are determined by the local field-strength, which is expected to be controlled by the externally applied discharge gap voltage. Experimentally, we replaced our usual solid anode with a segmented and transparent anode. With coincident high speed videography, the time-dependent anode segment currents allow us to unambiguously confirm the mode and direction of the rotating, self-organized coherent structures. Interestingly, the segmented anode current data reveal the existence of a stochastic regime between voltage-controlled mode transitions. An analysis of the segment currents in this regime indicates that the lower frequency coherent state decays into a spectrum of higher

frequency states that exhibit features consistent with a three-wave parametric mixing process.

The paper is presented as follows. In Sec. II, we describe the experimental setup. In Sec. III, we lay out the equations for the fluid model, with perturbation analysis, linearization, and the corresponding Fourier analysis giving rise to the dispersion relation for the linear modes. In Sec. IV, we describe the process of growth and formation of coherent instabilities by studying the dispersion relation for base conditions typical of our experiments. Then, we describe the experimental results and make comparisons to the model predictions. We also examine the role played by the drift-wave driven fluctuations in establishing the cross-field transport. In Sec. V, we discuss the observed dispersion and the dynamical behavior between coherent modes, in particular, those cases that show a clear evidence of three-wave interactions. Finally, in Sec. VI, we draw conclusions and make suggestions for future work.

II. EXPERIMENTAL SETUP

With the exception of the anode segments, the experimental facility is similar to that described previously.²⁰ A schematic is presented in Fig. 1. The main body of the small magnetron discharge consists of a 17 mm diameter samarium-cobalt (SmCo) permanent ring magnet with an iron (Fe) core. The magnet is covered and protected by a 120 μm thick graphite cathode. Graphite was selected for its low sputter yield. The generated magnetic field topology is simulated with a finite element solver²⁷ and is shown overlaid (as field lines and color are mapped for magnitude) on the discharge gap in the figure. The toroidal field is uniform in the azimuthal direction but varies strongly between the powered cathode and grounded anode. The maximum field at the cathode is approximately 1 T, falling to a 0.5 T halfway between the electrodes. This produces an axial field gradient $\partial B_0 / \partial x \approx 0.5 \text{ T mm}^{-1}$ or a characteristic field decay length $L_B = \partial(\ln B_0 / \partial x)^{-1} \approx 0.5 \text{ mm}$. Gradients along the radial direction are comparable to those along the axis, a condition which holds in the presence of the discharge current densities ($J \approx 10^3 \text{ A/m}^2$) encountered in our experiments.

The plasma forms as a toroid between the graphite cathode and a transparent, segmented, indium tin oxide (ITO) anode, close to where the field is the strongest near the boundary between the underlying iron core and SmCo ring magnet. In this region, the B-field lines are largely radial in their direction and eventually terminate directly on the graphite cathode. The transparent anode provides a direct optical access for high speed videography of the dynamics inferred from spectrally integrated plasma emission. Nevertheless, the anode is inevitably covered due to sputtering at the cathode surface, thus limiting the operation to only a few minutes before the ITO anode needs to be replaced. When viewed by the naked eye, the plasma appears to be quiescent, and ring-shaped, with the most luminous region closer to the cathode.²⁰ While recording anode segment currents, a high framing rate intensified CCD camera (Cordin, Model 222C-16UV) captures time-varying plasma emission through the ITO anode, as shown in the example frame at the top right of the figure. The camera can capture as many as 16 successive frames with exposure times of 0.5 μs and at a framing rate as high as 2.7 MHz. As shown in the representative camera frame, the anode is segmented into four

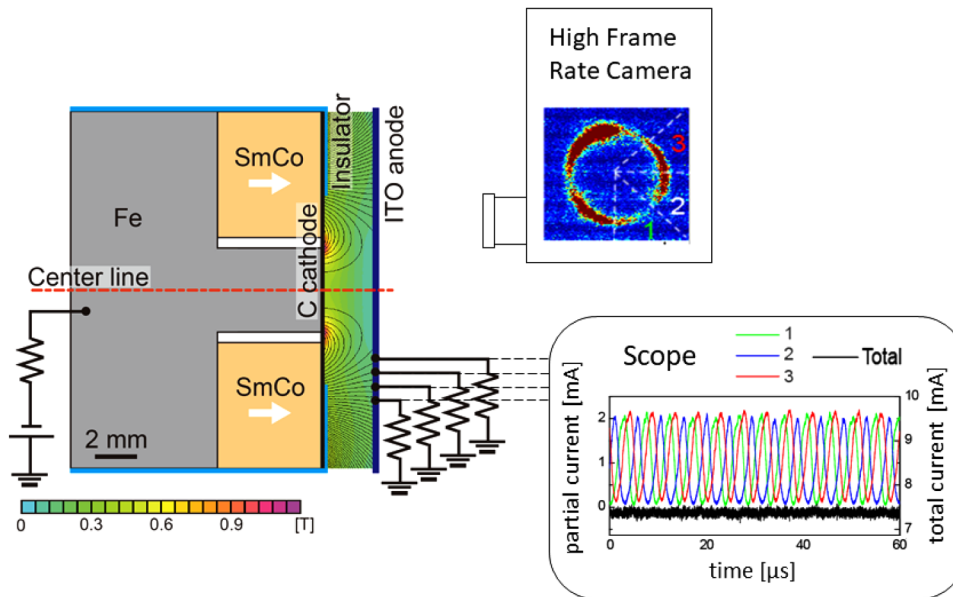


FIG. 1. Schematic of the setup. A graphite cathode covers and protects the magnet. The plasma emission is inspected through a transparent, segmented anode by a high speed camera. The representative discharge currents, collected by the segments, are shown along with the total current.

regions. Three smaller segments (45° apart) are used, together with the recorded high speed videos to discern the general plasma structure shape, the disturbance wavenumber, and the frequency. The current through the remaining fourth segment, together with the smaller three segments, is combined to provide a measure of the total discharge current. A $10\text{ k}\Omega$ ballast resistor is used to limit the current flow in the discharge (the left-hand side in Fig. 1), while four small shunt resistors are used to measure current fluctuating through the segments. In Fig. 1, an example of the segment current traces is given for the $m = 3$ coherent mode depicted in the camera frame shown (here, $m = k_y R_0$, with k_y being the azimuthal wavenumber of the disturbance and R_0 being the plasma radius). The values of the shunt resistors are sized so that the potential is uniform on the anode surface. The magnetron discharge operates in a vacuum chamber with argon as the working gas, controlled in pressure to 150 mTorr for all the data presented in this work. The discharge gap size is typically 2 mm .

III. DRIFT-WAVE INSTABILITY MODEL

The model used to interpret the dynamical behavior of the plasma starts from a two-fluid description similar to that of Perez *et al.*¹³ Externally applied electric and magnetic fields that act on the fluids are assumed to be static, and field coupling between the fluids is through an assumption of quasi-neutrality. The equations are perturbed, linearized, and Fourier analyzed to obtain the dispersion relation that governs azimuthal disturbances. In the model's implementation, we unfold the annular geometry of the magnetron to a Cartesian coordinate system (see Fig. 2). The axial electric field arising due to the externally applied voltage is E_x (x -direction, positive from anode to cathode), and the magnetic field, B_z , is taken to be primarily along the z -direction (radially inward). The background, undisturbed plasma is assumed to be

uniform in the azimuthal direction, which is the y -direction in the unfolded Cartesian coordinate frame, and contains a plasma density (n_0) and magnetic field gradients along the x -direction, as illustrated qualitatively in Fig. 2. We presume that the strongest ionization and emission occur just beyond the cathode fall where plasma density gradients produce a field reversal, $E_x < 0$, driving ions toward the anode. An analogous reverse ion migration was measured by laser induced fluorescence in the near anode region of Hall thrusters.²⁸

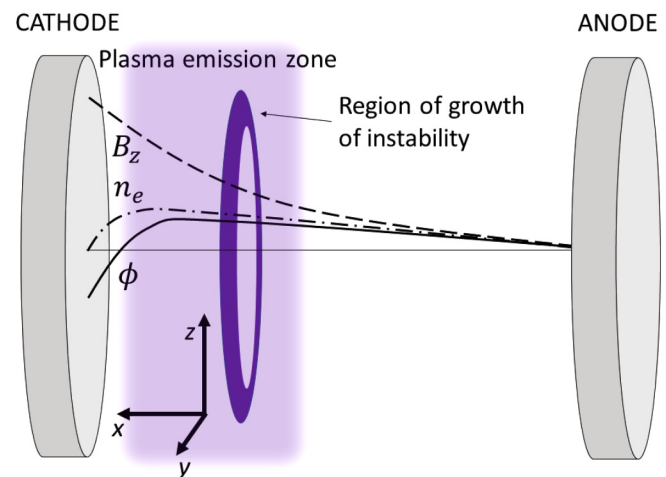


FIG. 2. Schematic of the toroidal plasma structure and the reference frame used in the model analyses, with illustrative profiles of magnetic field B_z , plasma density n_e , and plasma potential ϕ .

A. Electron dynamics

The electron fluid motion is described by the equations of particle and momentum conservation, which in the magnetized limit are expressed as

$$\frac{\partial n_e}{\partial t} + \nabla \cdot (n_e \mathbf{v}_e) = S_e, \quad (1)$$

$$m_e n_e \left(\frac{\partial}{\partial t} + \mathbf{v}_e \cdot \nabla \right) \mathbf{v}_e = -\nabla p_e - en_e (\mathbf{E} + \mathbf{v}_e \times \mathbf{B}) + \mathbf{R}_e. \quad (2)$$

Here, S_e is the ionization source term for the electron fluid, and \mathbf{R}_e represents the electron frictional force parallel to the magnetic field lines. Neglecting electron inertia and pressure gradients and approximating the macroscopic electron motion by their guiding center drift (justified by the relatively large electron gyrofrequency), we can express the electron drift velocity along the direction perpendicular to the magnetic field, $\mathbf{v}_{e\perp}$, as

$$\mathbf{v}_{e\perp} = \mathbf{v}_{E \times B} + \mathbf{v}_{eD},$$

where

$$\mathbf{v}_{E \times B} = \frac{\mathbf{E} \times \mathbf{B}}{B^2}; \text{ and } \mathbf{v}_{eD} = \frac{\nabla p \times \mathbf{B}}{en_e B^2} \quad (3)$$

represent the usual electron $E \times B$ drift velocity and the diamagnetic drift velocity, respectively. With the expression for $\mathbf{v}_{e\perp}$ above, we can reformulate the electron continuity equation in terms of perpendicular and parallel contributions, i.e.,

$$\frac{\partial n_e}{\partial t} + \nabla \cdot (n_e \mathbf{v}_{e\perp}) + \nabla \cdot (n_e \mathbf{v}_{e\parallel}) = \alpha_I n_e. \quad (4)$$

In the approach described in Perez *et al.*,¹³ $n_e \mathbf{v}_{e\parallel}$ is modeled as an effective diffusion term proportional to the density gradient along the B-parallel direction. We take a similar approach here and introduce a field-aligned effective diffusion coefficient D_{eff} . We note, however, the peculiarity of our magnetic topology in that the field lines in the vicinity of where the plasma forms (see Fig. 1) terminate back on the cathode. In general, this term can provide either a sink or a source of electrons. At this time, we simply parameterize this term together with that which describes the local ionization. We model the ionization term to be proportional to the plasma density through the ionization rate coefficient, α_I ; i.e., $S_e = \alpha_I n_e$. Assuming pressure gradients are driven primarily through gradients in plasma density (isothermal electrons), substitution of the expression for the above perpendicular component of the electron velocity into Eq. (4) gives

$$\frac{\partial n_e}{\partial t} + \mathbf{v}_{E \times B} \cdot \nabla n_e - 2n_e (\mathbf{v}_{E \times B} + \mathbf{v}_{eD}) \cdot \nabla \ln B_0 + \nabla \cdot \mathbf{\Gamma}_{\parallel} = \alpha_I n_e, \quad (5)$$

with

$$\mathbf{\Gamma}_{\parallel} = n_e \mathbf{v}_{e\parallel} = -D_{eff} \nabla_{\parallel} n_e.$$

Equation (5) describes the electron drift dynamics and includes both continuity and momentum equations. Again, the coefficient introduced as D_{eff} accounts for the electron loss ($D_{eff} > 0$) or gain ($D_{eff} < 0$) along the magnetic field lines. In general, B-parallel electron and ion motion can play an important role in the dynamics of the plasma. Even more important is the presence of sheaths when the plasma is bounded by a dielectric wall,²⁹ as is the case in Hall discharges, and a proper account for the current balance at this sheath is necessary. As pointed out above, in our discharge, the field lines in the region close to where the plasma is most dense intersect the cathode, and therefore, the field-aligned electron diffusion will be greatly affected by the conditions (e.g., electron emission) at the cathode surface, which at this time, we do not model. Because of this, the field-aligned flux term that includes D_{eff} is combined with the ionization coefficient, α_I , to define an adjustable parameter (see below) in the evaluation of the model for comparison to experiments.

B. Ion dynamics

The ion continuity and momentum equations in the non-magnetized case are

$$\frac{\partial n_i}{\partial t} + \nabla \cdot (n_i \mathbf{v}_i) = S_i, \quad (6)$$

$$m_i n_i \left(\frac{\partial}{\partial t} + \mathbf{v}_i \cdot \nabla \right) \mathbf{v}_i = -\nabla p_i + en_i \mathbf{E} + \mathbf{R}_i. \quad (7)$$

Here, \mathbf{R}_i represents the frictional force experienced by the ions due to scattering collisions, and $S_i = S_e$. As the ions are assumed to be non-magnetized, we consider here just the ion motion along the direction perpendicular to the B-field, i.e., along the axial direction parallel to the electric field. As mentioned earlier, we assume that the plasma is quasi-neutral ($n_e = n_i$), that the electric field is irrotational (introduce the plasma potential, ϕ), we neglect the ion pressure term (low ion temperature), and we neglect ion scattering collisions for motion along this direction. The resulting ion particle and momentum conservation equations reduce to

$$\frac{\partial n_e}{\partial t} + n_e \nabla \cdot \mathbf{v}_{i\perp} + \mathbf{v}_{i\perp} \cdot \nabla n_e = \alpha_I n_e, \quad (8)$$

$$m_i n_e \left(\frac{\partial}{\partial t} + \mathbf{v}_i \cdot \nabla \right) \mathbf{v}_i = -en_e \nabla \phi. \quad (9)$$

C. Perturbation and linearization

With the magnetic field at the axial location of interest, $B_z \approx B_0$, Eq. (5) can be expressed explicitly using the coordinate system

adopted (shown in Fig. 2) as

$$\begin{aligned} \frac{\partial n_e}{\partial t} - \frac{1}{B_0} \frac{\partial \phi}{\partial y} \frac{\partial n_e}{\partial x} + \frac{1}{B_0} \frac{\partial \phi}{\partial x} \frac{\partial n_e}{\partial y} \\ - 2n_e \frac{\partial \ln B}{\partial x} \left(\frac{k_B T_e}{en_e B_0} \frac{\partial n_e}{\partial y} - \frac{1}{B_0} \frac{\partial \phi}{\partial y} \right) \\ - D_{\text{eff}} \frac{\partial^2 n_e}{\partial z^2} = \alpha_I n_e. \end{aligned} \quad (10)$$

We begin the analysis by representing the dynamic fluctuations in plasma density and plasma potential as perturbations on a base equilibrium plasma that is uniform in the azimuthal direction:

$$\begin{aligned} n_e = n_0 + n_1, \quad \phi = \phi_0 + \phi_1, \\ \frac{\partial n_0}{\partial y} = 0, \quad \frac{\partial \phi_0}{\partial y} = 0. \end{aligned}$$

We introduce characteristic lengths to approximate gradients of zeroth order quantities in the axial direction,

$$\frac{\partial \ln B_0}{\partial x} = \frac{1}{L_B}, \quad \frac{\partial \phi_0}{\partial x} = -E_0, \quad \frac{\partial n_0}{\partial x} = \frac{n_0}{L_n}.$$

After substitution into Eq. (10) and since the base case satisfies the unperturbed electron particle and momentum conservation equations, we arrive at the following equation for the electron (ion) perturbation amplitudes:

$$\begin{aligned} \frac{\partial n_1}{\partial t} - \left(\frac{E_0}{B_0} + \frac{2k_B T_e}{eB_0 L_B} \right) \frac{\partial n_1}{\partial y} \\ - \left(\frac{n_0}{B_0 L_n} - \frac{2n_0}{B_0 L_B} \right) \frac{\partial \phi_1}{\partial y} - D_{\text{eff}} \frac{\partial^2 n_1}{\partial z^2} - \alpha_I n_1 \\ + \left\{ \frac{1}{B_0} \frac{\partial n_1}{\partial y} \frac{\partial \phi_1}{\partial x} - \frac{1}{B_0} \frac{\partial n_1}{\partial x} \frac{\partial \phi_1}{\partial y} + \frac{2n_1}{B_0 L_B} \frac{\partial \phi_1}{\partial y} \right\} = 0. \end{aligned} \quad (11)$$

The expression within curly brackets represents the nonlinear dynamic, which we will neglect moving forward. However, for future analyses, these terms can be retained to examine the nonlinear behavior of the system as it pertains to the parametric mixing that is described later in Sec. V. We note that by neglecting the nonlinear terms, the analysis presented here is only able to describe the initial growth of the instabilities. A proper analysis of the dynamics, particularly as it pertains to the parametric mixing, may require a solution of the full fluid equations, as recently carried out by Smolyakov *et al.*³⁰

For the ions, Eq. (8) can be expressed in terms of the coordinate system adopted as

$$\frac{\partial n_e}{\partial t} + n_e \frac{\partial v_x}{\partial x} + v_x \frac{\partial n_e}{\partial x} + n_e \frac{\partial v_y}{\partial y} + v_y \frac{\partial n_e}{\partial y} = \alpha_I n_e. \quad (12)$$

Here, we have dropped the subscript *i* as all velocities from here on refer to those of the ions. As above, we express the velocities in

terms of perturbation of their base values,

$$v_x = v_{x_0} + v_{x_1}, \quad v_y = v_{y_0} + v_{y_1}.$$

We take the base ion velocities to have the following properties:

$$\frac{\partial v_{x_0}}{\partial x} = 0, \quad v_{y_0} = 0, \quad \frac{\partial v_{y_0}}{\partial y} = 0.$$

In making these assumptions, we are implying that the ions are sufficiently heavy that they do not drift in the azimuthal direction. We further assume that within the region in which we see strong fluctuations, the ions drift along the axial direction with a constant ion velocity. As discussed above, this ion velocity will be taken to be anode-directed due to the presence of a field reversal within the gap. We also neglect ionization in the ion continuity equation because estimates place it to be much smaller than the frequencies of interest. With these assumptions, and with the gradient length scales describing the axial variation in the base plasma density, L_n , Eq. (12) reduces to

$$\begin{aligned} \frac{\partial n_1}{\partial t} + n_0 \frac{\partial v_{x_1}}{\partial x} + \frac{v_{x_1} n_0}{L_n} + v_{x_0} \frac{\partial n_1}{\partial x} + n_0 \frac{\partial v_{y_1}}{\partial y} \\ + \left\{ n_1 \frac{\partial v_{x_1}}{\partial x} + v_{x_1} \frac{\partial n_1}{\partial x} + n_1 \frac{\partial v_{y_1}}{\partial y} + v_{y_1} \frac{\partial n_1}{\partial y} \right\} = 0. \end{aligned} \quad (13)$$

Here, once again, we assumed that the quiescent base plasma properties satisfy the ion particle and momentum conservation equations. As in the equations for the electrons, the expression within curly brackets represents the non-linear terms, which will be neglected moving forward but can be re-visited in future analyses.

We now turn to the ion momentum equations. Starting with the axial direction (*x*) and using the convention defined in Fig. 2, we have

$$v_x \frac{\partial v_x}{\partial x} + \left(v_y \frac{\partial v_x}{\partial y} + v_z \frac{\partial v_x}{\partial z} \right) = -\frac{e}{m_i} \frac{\partial \phi}{\partial x} - \frac{\partial v_x}{\partial t}. \quad (14)$$

Similarly, for the azimuthal (*y*) direction, we write

$$v_y \frac{\partial v_y}{\partial y} + \left(v_x \frac{\partial v_y}{\partial x} + v_z \frac{\partial v_y}{\partial z} \right) = -\frac{e}{m_i} \frac{\partial \phi}{\partial y} - \frac{\partial v_y}{\partial t}. \quad (15)$$

When substituting the perturbed expressions for the velocities, and within the framework of the above assumptions, we arrive at the following equations for the *x* and *y* perturbation amplitudes:

$$v_{x_0} \frac{\partial v_{x_1}}{\partial x} + \left\{ v_{y_1} \frac{\partial v_{x_1}}{\partial y} + v_{z_1} \frac{\partial v_{x_1}}{\partial z} \right\} = -\frac{e}{m_i} \frac{\partial \phi_1}{\partial x} - \frac{\partial v_{x_1}}{\partial t}, \quad (16)$$

$$v_{x_0} \frac{\partial v_{y_1}}{\partial y} + \left\{ v_{x_1} \frac{\partial v_{y_1}}{\partial x} + v_{z_1} \frac{\partial v_{y_1}}{\partial z} \right\} = -\frac{e}{m_i} \frac{\partial \phi_1}{\partial y} - \frac{\partial v_{y_1}}{\partial t}. \quad (17)$$

In Eqs. (16) and (17), again, the expressions within curly brackets represent the nonlinear terms, which will be neglected henceforth.

D. Fourier analysis

Neglecting nonlinear terms, we express the perturbations in the usual form as fluctuations in space and time,

$$\psi = \delta\psi \exp[i(k_x x + k_y y + k_z z - \omega t)]. \quad (18)$$

Here, k_x , k_y , and k_z represent the component wavenumbers of the disturbance and ω the frequency. We will assume real axial (x) and radial (z) wavenumbers and solve for the frequency and growth rate of the temporal instability as a function of the azimuthal (y) wavenumber. By doing so, we are assuming that the disturbances along the three principal directions are independent of each other, which can only be true in the linear limit. Nothing can be inferred about nonlinear effects as we neglect all nonlinear terms in the perturbation equations.

This analysis applied to Eq. (11) leads to the perturbation amplitude in the plasma density,

$$\frac{\delta n}{n_0} = \frac{\omega^* - \omega_D}{\omega - \omega_0 - \omega_D + i(k_z^2 D_{eff} - \alpha_I)} \frac{e\delta\phi}{k_B T_e}, \quad (19)$$

where for the sake of simplicity, we defined the following characteristic frequencies:

$$\omega_0 = -k_y \frac{E_0}{B_0}, \quad \omega_D = -k_y \frac{2k_B T_e}{eB_0 L_B}, \quad \omega^* = -k_y \frac{k_B T_e}{eB_0 L_n}.$$

In a similar way, the axial and azimuthal ion momentum equations [Eqs. (16) and (17)] become

$$\delta v_{x1} = \frac{\frac{e}{m_i} k_x}{\omega - k_x v_{x0}} \delta\phi, \quad \delta v_{y1} = \frac{\frac{e}{m_i} k_y}{\omega - k_x v_{x0}} \delta\phi. \quad (20)$$

For the ion continuity equation, we assume that $\frac{1}{L_n} \ll k_x$ (i.e., the density gradient length scale is taken to be large in comparison with the component wavelength in the axial direction). With this assumption and with the use of Eq. (19), the ion continuity leads to the following for the perturbation amplitude in the plasma density:

$$\frac{\delta n}{n_0} = \frac{c_s^2 k_\perp^2}{(\omega - k_x v_{x0})^2} \frac{\delta\phi}{k_B T_e/e}, \quad (21)$$

where we have defined $k_\perp^2 = k_x^2 + k_y^2$ and $c_s = \sqrt{\frac{k_B T_e}{m_i}}$ is the usual ion sound speed in the plasma.

E. Wave dispersion

By equating Eqs. (19) and (21), we obtain the wave dispersion relation,

$$\omega^2 - \left(2k_x v_{x0} + \frac{c_s^2 k_\perp^2}{\omega^* - \omega_D}\right) \omega + k_x^2 v_{x0}^2 + \frac{c_s^2 k_\perp^2 (\omega_0 + \omega_D)}{\omega^* - \omega_D} - i \frac{k_\perp^2 c_s^2 v_c}{\omega^* - \omega_D} = 0. \quad (22)$$

Here, in the imaginary term of the equation, $v_c = k_z^2 D_{eff} - \alpha_I$ collects the effects of ionization and plasma loss along the magnetic

field direction and represents an *ad hoc* parameter that is adjusted in the model, as mentioned earlier. Equation (22) is a second order polynomial with complex coefficients resulting in complex solutions $\omega = \omega_R + i\omega_I$, where

$$\begin{aligned} \omega_R = & \frac{1}{2} \left(2v_{x0} k_x + k_\perp^2 \frac{c_s^2}{\omega^* - \omega_D} \right) \\ & + \frac{1}{2\sqrt{2}} \left\{ \left[\frac{c_s^8 k_\perp^8}{(\omega^* - \omega_D)^4} + 8 \frac{v_{x0} k_x - \omega_0 - \omega_D}{(\omega^* - \omega_D)^3} c_s^6 k_\perp^6 \right. \right. \\ & \left. \left. + 16 \frac{(v_{x0} k_x - \omega_0 - \omega_D)^2 + v_c^2}{(\omega^* - \omega_D)^2} c_s^4 k_\perp^4 \right]^{\frac{1}{2}} \right. \\ & \left. + \frac{c_s^4 k_\perp^4}{(\omega^* - \omega_D)^2} + 4 \frac{v_{x0} k_x - \omega_0 - \omega_D}{\omega^* - \omega_D} c_s^2 k_\perp^2 \right\}^{\frac{1}{2}}, \quad (23) \end{aligned}$$

$$\begin{aligned} \omega_I = & + \frac{1}{2\sqrt{2}} \left\{ \left[\frac{c_s^8 k_\perp^8}{(\omega^* - \omega_D)^4} + 8 \frac{v_{x0} k_x - \omega_0 - \omega_D}{(\omega^* - \omega_D)^3} c_s^6 k_\perp^6 \right. \right. \\ & \left. \left. + 16 \frac{(v_{x0} k_x - \omega_0 - \omega_D)^2 + v_c^2}{(\omega^* - \omega_D)^2} c_s^4 k_\perp^4 \right]^{\frac{1}{2}} \right. \\ & \left. - \frac{c_s^4 k_\perp^4}{(\omega^* - \omega_D)^2} - 4 \frac{v_{x0} k_x - \omega_0 - \omega_D}{\omega^* - \omega_D} c_s^2 k_\perp^2 \right\}^{\frac{1}{2}}. \quad (24) \end{aligned}$$

IV. COHERENT INSTABILITIES

A. Formation and growth

In the absence of the field-aligned diffusion and ionization, the wave dispersion [Eq. (22)] will have identical characteristics to that derived by Frias *et al.*,²² and with E_0 (and v_{x0}) < 0, the region of instability has a distinct long wavelength cutoff that depends on background plasma conditions. As previously mentioned, we assume that all quantities are known except for the azimuthal wavenumber k_y . This will allow us to express the complex frequency as a function of the azimuthal wavenumber. As usual, the real part of ω [Eq. (23)] describes the dispersion of the disturbance, while the complex part [Eq. (24)] describes its initial growth rate. We seek, for a set of plasma properties, the azimuthal wavenumbers that give rise to positive imaginary contributions to the roots, as they are the ones that lead to a positive growth in the disturbances. Positive real contributions to the frequency correspond to a propagation direction opposite that of the $E \times B$ direction.

As an example, in Fig. 3, we plot the modeled growth rate vs the non-dimensionalized wavenumber (mode number), $m = k_y R_0$, of the unstable branch. In doing so, we use plausible experimental conditions $L_n = 2$ mm, $B_0 = 0.6$ T, $2\pi/k_x = 2.5$ mm, and $2\pi/k_z = 0.9$ mm. We take $v_c = 5 \times 10^7$ s⁻¹, chosen to reproduce experimental trends as discussed below. As mentioned earlier, pinning it down will require understanding the interaction of the plasma with the cathode at the terminal ends of the field lines. The local axial electric field, E_0 , which is assumed to depend linearly with the discharge gap voltage, is varied to sample a range of local

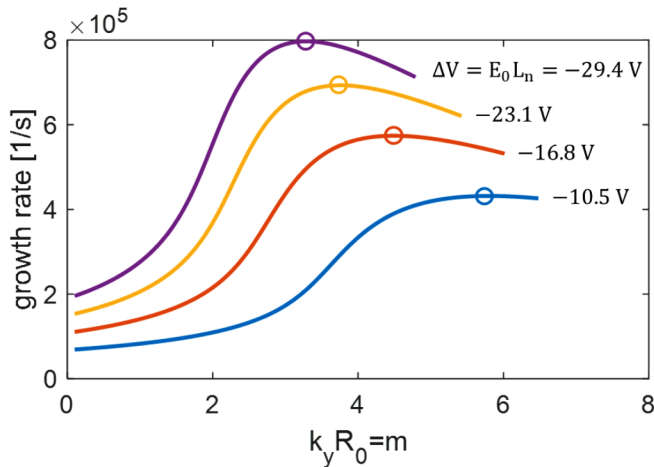


FIG. 3. Growth rate variation with the azimuthal wavenumber (mode number) computed for a range of values of the reverse-field potential.

field-reversed potentials, defined as $\Delta V = E_0 L_n$. In doing so, we scale the values of the local ion velocity and electron temperature to the local field using $v_{i0} \sim E_0^{1/2}$ and $k_B T_e \sim E_0$. As a reference, for $\Delta V = -23.1$ V, taken to correspond to a discharge gap voltage of 272 V, $v_{i0} = -933$ m/s and $k_B T_e = 3.1$ eV—also parameters that are largely unknown but reasonable and should be validated by future experiments.

For these conditions, we see from Fig. 3 that the maximum in the linear growth rate, which we presume may determine the preferred mode numbers, are in the range $m = 3-5$, and increase with a decrease in the local value of the electric field (or field-reversal potential). Determining the conditions that define instability from Eq. (22) is made difficult by the presence of the imaginary term. We will see in Sec. IV E how, for our conditions, where there is a field reversal within the gap and positive values of L_n and L_B , instability requires $2L_n > L_B$ and L_B to be greater than a threshold value \bar{L}_B . Because of the finite value of v_c , the system is unconditionally unstable; i.e., it is unstable over all wavelengths with no lower wavelength cutoff when these conditions on the gradient length scales are met. In practice, as described above, we assume that the field-reversal potential will scale linearly with the applied discharge gap voltage—a feature that should be validated by future experiments or computational simulations. We would expect that high discharge voltages will generate high plasma densities and hence higher (positive) values of ΔV . This would predict that higher mode numbers are expected at lower voltages. The model also predicts that mode transitions should occur with a hysteresis if the discharge voltage is swept without interruption, with higher modes favored over lower modes as voltages are increased and lower modes favored over higher modes when voltages are decreased. For example, with increasing discharge voltage, conditions that favor an active $m = 4$ mode will persist until the peak growth rate surpasses a critical value, triggering a mode transition to $m = 3$. Reversing the voltage should maintain the $m = 3$ mode until a transition to $m = 4$ occurs at some higher voltage. In the

experiments presented below, we do not sweep voltage continuously and instead initiate the plasma from a cold start at various discharge voltages to limit the on-time of the discharge in order to avoid erosion of the thin indium tin oxide coating on the transparent anode. A study of the existence of a discharge hysteresis is the subject of future work and its presence would be further validation of the model.

B. Experimental results

The high framing rate movies taken through the transparent anode allowed for direct capture of the rotation frequency and wave mode of the coherent structures as discharge conditions are varied. Figure 4 plots as symbols the experimentally measured frequencies (delineated by the favored modes) over a 20 V range in the discharge voltage (corrected for the ballast voltage drop). The results from the model are overlaid as a function of the potential $E_0 L_n$ (top axis), also varying in range by 20 V. To overlay the experimental data, we assume a $\Delta V = 30$ V potential reversal when the gap voltage is 279 V.

We see from the figure that the model is able to capture the general trends seen in the experiments. It is noteworthy that it predicts two somewhat counter-intuitive features seen in the experiments. The first is that within a given azimuthal mode, the frequency of the instability decreases with increasing discharge voltage even though higher voltages (and hence higher values of the local field) are expected to generate higher $E \times B$ velocities. The second is that the frequency of the instability increases with a decrease in the favored mode number. This implies that the phase velocity of the wave increases with increasing wavelength. These features are, of course, a consequence of the wave dispersion, which is depicted in Fig. 5 for the range of field-reversed potentials shown in the previous figure. For any given value of the field-reversed

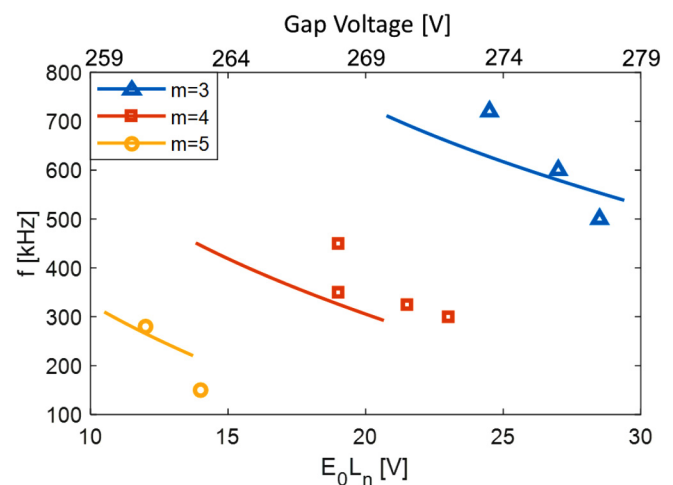


FIG. 4. Mode frequencies from experiments (symbols) and predicted by the analysis (lines) as a function of the experimental discharge voltage (lower abscissa) and modeled $E_0 L_n$ due to field reversals (upper abscissa). The scales are matched assuming a 30 V voltage hump when the discharge voltage is 279 V.

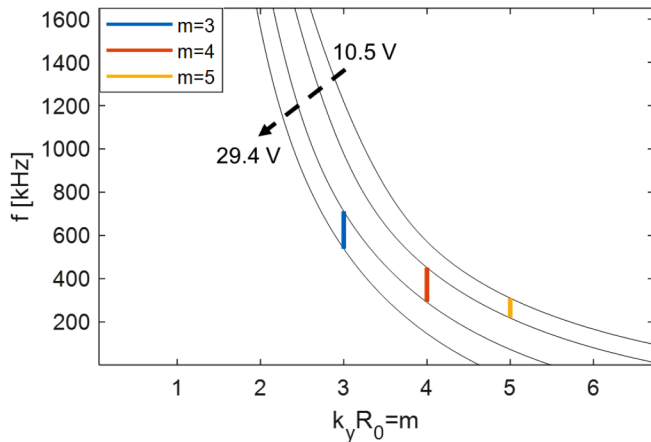


FIG. 5. Wave dispersion arising from the model for various values of the field-reversed potential. Regions are highlighted depicting the range in which various azimuthal modes are preferred (have the greatest linear growth rates).

potential, the frequency decreases with increasing wavenumber (decreasing wavelength). The reason for this is discussed in detail in Sec. IV D. The wavenumber-dependence of the real part of the unstable root of Eq. (22) is dominated by the linear term, which is comprised of two parts—that which depends on the ion velocity and insensitive to wavelength (as k_x is taken to be constant) and that which is nearly inversely dependent on k_y , since $k_x \gg k_y$. Since only discrete sets of wavelengths establish the resonant modes of the system, when anchored to a particular mode ($m = 5$, in this case), an increase in operating discharge potential will lead to a reduction in the frequency (decrease in the phase velocity). Beyond some limit, a further increase in discharge potential favors a lower-order mode, resulting in a mode transition and a change (increase) in the phase velocity, a pattern that will continue as the system passes through multiple states.

As previously mentioned, a combination of anode segment current measurements and a comparison of high speed video-graphic imaging through the anode allow for the unambiguous determination of the frequency and the mode number. The current segments alone are not enough to precisely determine the mode number because the spatial resolution is limited by the segment area. For example, with 45° segments, modes higher than $m = 4$ will not be properly resolved by the current measurements alone due to aliasing. An example of how the determination is carried out for when the discharge is in states corresponding to $m = 3$ and $m = 4$ modes is illustrated with the help of Figs. 6 and 7, respectively. In these figures, the location of the anode segments (1–4) is shown in the images, and their corresponding collected currents are shown in the central plot. We note that the current measurements are delayed with respect to the density fluctuation because of the time of flight of charged particles and the different phase shifts of ion and electron velocities.

It is apparent that aliasing is not a factor in the current traces seen in Fig. 6, as they are well resolved in time, and the direction of

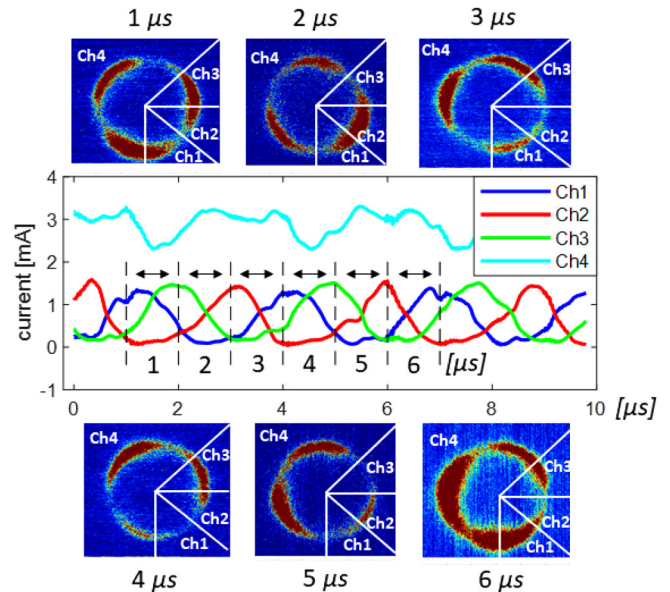


FIG. 6. Comparison between current measurements and anode pictures for $m = 3$. The sampling frequency for current measurements is 250 MHz. A 25-point moving average filter is applied to reduce noise. The exposure time is 1μ s for each frame. The delay time, measured from $t = 0$ to the moment of sensor exposure, is shown for each frame and is indicated in the current traces.

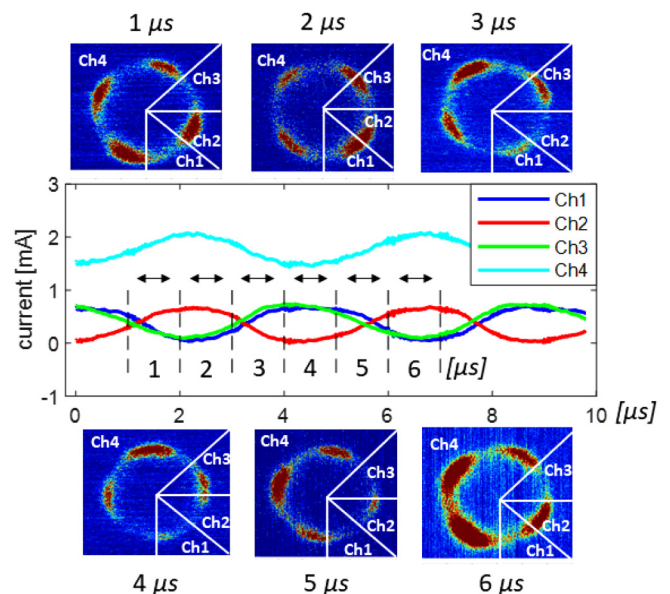


FIG. 7. Comparison between current measurements and anode pictures for $m = 4$. Camera settings and other considerations are the same as in Fig. 6.

rotation is readily established. For example, from the current traces, we see that the current through segment 3 (channel 3) precedes that of segment 2 (channel 2), which precedes that of segment 1 (channel 1). Therefore, we conclude that the plasma rotates clockwise (as viewed in the image) and confirmed by the time sequence of the images. A clockwise rotation of the plasma structures confirms that a structure straddling segment 3 will straddle segment 1 $2\ \mu\text{s}$ later (frames labeled $1\ \mu\text{s} - 3\ \mu\text{s}$), as seen in the current traces. However, an assumed counterclockwise rotation of the plasma structure that straddles segment 1 (see the frame labeled $3\ \mu\text{s}$, channel 1) would arrive at segment 3 (frame labeled $4\ \mu\text{s}$, channel 3) $1\ \mu\text{s}$ later—a result inconsistent with the current traces. In contrast, the problem of potential aliasing is clearly apparent in Fig. 7. There, we see that the currents collected from segments 1 and 3 have nearly identical forms (the same phase) and are indistinguishable due to the 90° separation between them. From the current traces, the current through segment 2 can be seen to precede that of segment 3 or segment 1; therefore, an analysis of just the current traces would be inconclusive in determining the direction of rotation. However, in combination with the video frames, we can confirm that the rotation of the plasma structures is clockwise. We see that if a structure straddles segment 2 (in the frame labeled $1\ \mu\text{s}$) and is rotating counterclockwise, it would arrive at segment 3 in less than $1\ \mu\text{s}$ —a result inconsistent with the current traces, which suggest that it takes two microseconds to do so. However if the same structure rotates clockwise, the video reveals that it straddles segment 1 two microseconds later (frame labeled $3\ \mu\text{s}$)—a result consistent with the current traces. In our experimental configuration, a clockwise rotation in these video frames represents a drift in the negative $E \times B$ direction (here, E is that field associated with the externally applied potential).

C. Sensitivity analysis

The free energy that drives the instability is the relative drift of the electrons and ions due to their disparate magnetization and the presence of field gradients. The many poorly experimentally quantifiable parameters in the model demand that we perform a sensitivity analysis to understand which parameters have a greatest impact on the formation and growth of the instability. The sensitivity analysis is performed numerically for the condition of $E_0L_n = -23.1\ \text{V}$, where the $m = 3$ mode seems to be preferred for decreasing voltages. We generally find that the formation of the instability is most sensitive to the magnetic field gradient (represented by the parameter L_B). A slight increase in the magnetic field gradient (e.g., by about 10%) nearly doubles the growth rate and shifts its peak to prefer higher mode numbers. A slight increase in ion mass and assumed reverse-field potential tend to shift the growth rates to prefer lower mode numbers, without a substantial increase in the peak growth rate. A slightly higher density gradient and a plasma radius shift growth rates to prefer higher mode numbers (also without a significant increase in the growth rate). These results can be used to anticipate the qualitative behavior of other operating conditions; for example, we might expect lower preferred mode numbers for heavier gases. Future experiments will attempt to confirm these scalings.

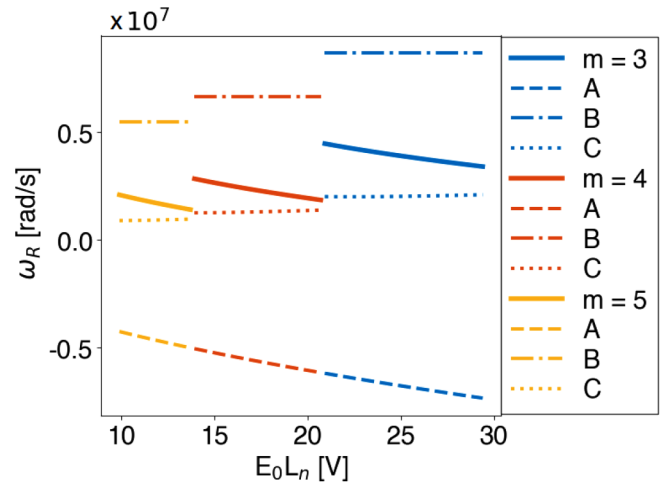


FIG. 8. Frequency of instability vs plasma potential for decreasing voltages decomposed in three contributions A, B, and C so that $\omega_R = A + B + C$.

D. Analysis of the terms in the analytical solution

The analytical expression of ω_R [Eq. (23)] can be decomposed into contributions A, B, and C, where $A = v_{x0}k_x$, $B = \frac{1}{2}k_\perp^2 c_s^2 / (\omega^* - \omega_D)$, and C is the more complicated term with two nested square roots so that $\omega_R = A + B + C$. Figures 8 and 9 show the contributions of the three terms to the total magnitude of ω_R for the same conditions as in Fig. 4 as a function of the field-reversal potential for the different modes (Fig. 8) and the wavenumber for a fixed potential (Fig. 9), respectively. As one can see, for our conditions, none of the three terms are negligible and the dispersion cannot be further simplified. As a result, it is instructive to understand the contributions that each term makes and their general behavior as operating conditions may be varied.

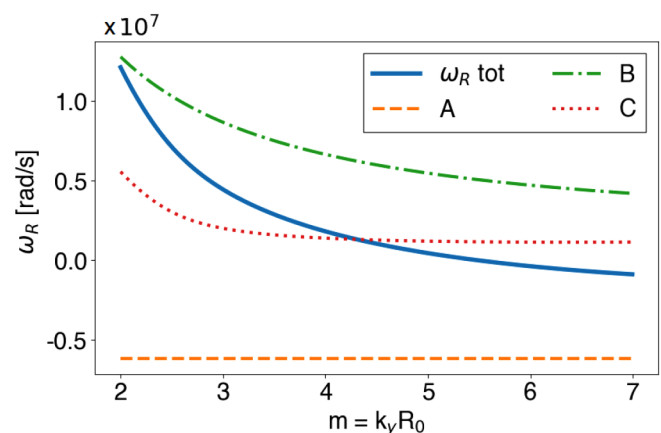


FIG. 9. Frequency of instability vs the wavenumber k_y for $E_0L_n = -21\ \text{V}$ decomposed in three contributions A, B, and C so that $\omega_R = A + B + C$.

The first term, A ($A = v_{x_0} k_x$), is generally responsible for the decreasing frequencies within modes (Fig. 8) as the discharge voltage is increased but does not contribute to the frequency separation between modes since it is not a function of k_y (Fig. 9). Its value is negative because v_{x_0} is negative (ions are leaving the plasma region toward the anode due to the presumed field reversal) and increases in magnitude with increasing discharge potential, while k_x is assumed to be constant. It is for this reason that the model predicts the counter-intuitive trend with discharge potential. If we were able to avoid this field reversal (by lowering the density gradient, for example), the model would predict increasing frequencies within modes and also higher frequencies, since all the other terms are positive. Future experiments will aim at validating this behavior.

Conversely, the term B is only a function of the wavenumber k_y and does not depend on the field reversal potential. This is because c_s^2 , ω^* , and ω_D are linear functions of the plasma temperature, and although T_e is modeled to depend on the field-reverse potential (which is presumed to vary linearly with discharge potential), T_e shows up as a linear term in both the numerator and denominator and so it cancels altogether. From Fig. 8, we see that B is responsible for the frequency separation between modes, with higher frequencies associated with lower mode numbers. Its variation scales nearly inversely with k_y because k_{\perp}^2 [defined in Eq. (21)] is a weak function of k_y (due to the dominating contribution from k_x).

The term C is important in magnitude to the final result (Fig. 8) but contributes less to the general trends. Curiously, A and B, being opposite in sign, almost cancel, leaving C to contribute substantially to the final values of the frequency. C would be negligible without the field reversal, leading to a much simplified expression for ω_R and much higher frequencies.

E. Conditions for instability

An inspection of the internal structure of C reveals that it is very similar to ω_I [Eq. (24)]. If we define $\beta = \frac{1}{8} c_s^4 k_{\perp}^4 / (\omega^* - \omega_D)^2$,

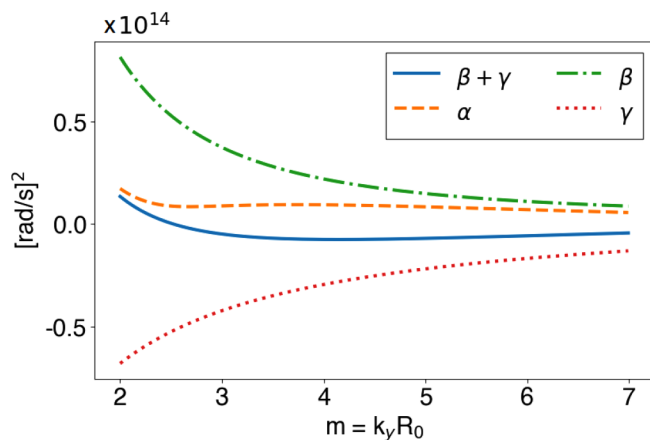


FIG. 10. For the same conditions as Fig. 9, terms α , β , and γ show how the formation of the maximum value of ω_I , necessary for the formation of a coherent instability, is due to the competition between β and γ .

$\gamma = \frac{1}{2}(v_{x_0} k_x - \omega_0 - \omega_D) / (\omega^* - \omega_D) c_s^2 k_{\perp}^2$ and α to be the third factor from the doubly nested square root, we can decompose C^2 and ω_I^2 so that $C^2 = \alpha + (\beta + \gamma)$ and $\omega_I^2 = \alpha - (\beta + \gamma)$. Figure 10 reveals that β dominates over γ at low wavenumbers and γ dominates over β at higher wavenumbers. This competition leads to a minimum in the sum $\beta + \gamma$, which is equivalent to a maximum in ω_I . A necessary condition for this competition to occur is for γ to be negative, since β is always positive. For this condition to hold, either the numerator or the denominator of γ must be negative. γ can be expressed as

$$\frac{\gamma}{c_s^2 k_{\perp}^2} = \frac{v_{x_0} k_x + k_y \frac{E_0}{B_0} + k_y \frac{2k_B T_e}{e B_0 L_B}}{-k_y \frac{k_B T_e}{e B_0 L_n} + k_y \frac{2k_B T_e}{e B_0 L_B}}. \tag{25}$$

We can study the sign of γ by studying the sign of the numerator and denominator of Eq. (25) in the presence or absence of a field reversal. The denominator is positive if $\frac{1}{L_n} < \frac{2}{L_B}$. The study of the sign of the numerator is more complicated because it depends on the field reversal (which in turn determines the sign of both E_0 and v_{x_0}), the sign of B_0 , and the geometrical parameter $\xi = \frac{k_x}{k_y}$. Interestingly, the numerator does not depend on L_n ; therefore, the effect of the numerator on the sign of γ can be described by a limiting L_B value,

$$\bar{L}_B = \frac{2k_B T_e}{|v_{x_0} | \xi B_0 + |E_0|}. \tag{26}$$

Figures 11 and 12 show the regions of instability in the L_B - L_n plane when $B_0 > 0$ in the presence and absence of field reversals, respectively.

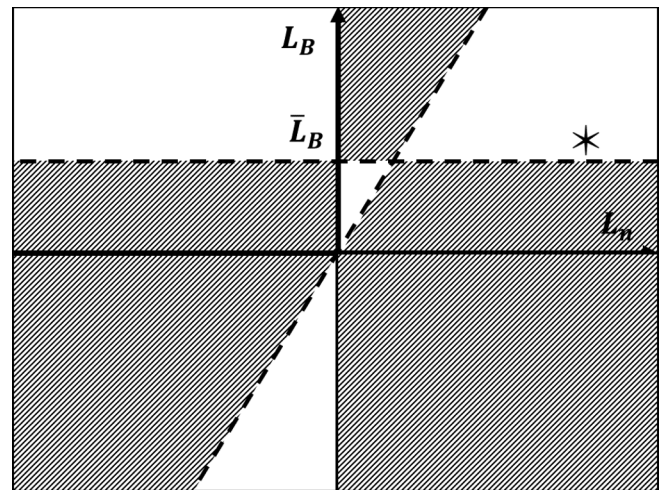


FIG. 11. Instability map in the presence of field reversals ($E_0 < 0$) and a positive magnetic field, where coherent instability regions are not gray. The experimental condition of the magnetron experiment discussed in this paper is indicated in the region of positive L_B and L_n , right above the \bar{L}_B limit. Under these conditions, the \bar{L}_B limit exists only for a positive L_B since the numerator of γ is always negative in the third and fourth quadrants.

Figure 12 shows the same instability region found by Frias *et al.*,²³ with the addition of a region for $-\bar{L}_B < L_B < 0$ where the condition reverses. Figure 11 is relevant to our experimental conditions because of the field reversal within the gap. In general, the value of \bar{L}_B can have a stabilizing or destabilizing effect on a discharge when we change the operating conditions. In particular, \bar{L}_B becomes larger in magnitude within modes for increasing E_0 and for decreasing ξ , giving rise to either a lower or higher threshold for the formation of the instability.

It is noteworthy that the conditions necessary for the SHI and MSHI (that do not account for magnetic field gradients); i.e., $\nabla n_e \cdot E_0 > 0$ are captured by our analyses in the limiting case. Indeed, our experiments violate this condition because of the density gradients and the local field reversal. As apparent in Fig. 11, our conditions, with $E_0 < 0$, generate an instability when $L_n > 0$. However, consistent with the conditions of the SHI and MSHI, we recover $\nabla n_e \cdot E_0 > 0$ for both $E_0 > 0$ (lower and upper right quadrants in Fig. 12) and $E_0 < 0$ (lower and upper left quadrants in Fig. 11) in the limit of a uniform magnetic field (i.e., $L_B \rightarrow \pm \infty$).

The conditions found by the stability analysis impose a constraint on the steepness of the gradient in the magnetic field, which can be controlled by the design of the magnetic topology. The density gradient is less easily controlled but perhaps can be influenced by the control of the discharge gap. We note, however, that the reversal in the midgap field is predicated upon the density gradient length scale, L_n , being small in order to drive excess electrons toward the anode by diffusion. Too low of a density gradient (or larger gap) is expected to result in waves that will reverse in their propagation direction, i.e., conform to that which is usually expected—the $E \times B$ direction determined by the external fields. As a result, this model suggests that there is a narrow window of

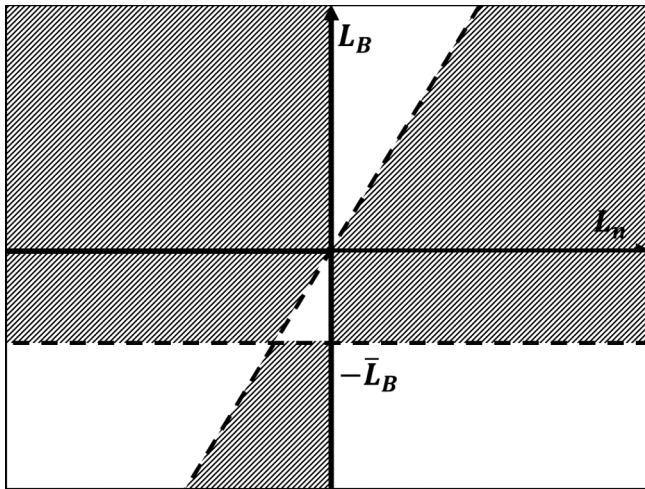


FIG. 12. Instability map in the absence of field reversals ($E_0 > 0$) and a positive magnetic field, where coherent instability regions are not gray. Under these conditions, the \bar{L}_B limit exists only for a negative L_B since the numerator of γ is always positive in the first and second quadrants.

opportunity in which coherent structures are driven to propagate in such retrograde directions.

F. Fluctuations and particle transport

Fluctuations are known to potentially drive or enhance electron and ion transport across magnetic field lines. The linear perturbation analysis described above provides some guidance as to conditions that must be established to be able to produce the correlated electron and ion density and axial velocity fluctuations, which may account for the measured time-varying and average anode current. Here, we estimate these electron and ion period-averaged current densities through the quasi-linear description (we revert back to using the subscripts e and i to specify species velocities),

$$\langle \delta J_{e_x} \rangle = -\frac{1}{2} \text{Re} \left\{ e \delta n \delta v_{e_x}^* \right\}, \quad (27)$$

$$\langle \delta J_{i_x} \rangle = \frac{1}{2} \text{Re} \left\{ e \delta n \delta v_{i_x}^* \right\}. \quad (28)$$

The superscript, $*$, denotes the complex conjugate of the perturbation amplitude. The perturbation in the electron axial velocity is due to the coupling of the induced azimuthal perturbation in plasma potential and pressure to the radial magnetic field, $\delta v_{e_{x \times B}}$ and $\delta v_{e_{x D}}$, respectively [from Eq. (3)]. Only the former gives a net nonzero contribution since $\delta v_{e_{x D}}$ is $\pi/2$ out of phase with respect to the density fluctuation; therefore, of the two, we will consider only $\delta v_{e_{x \times B}}$.

We can write the perturbation velocities as

$$\delta v_{e_x} = -ik_y \frac{\delta \phi}{B_0}, \quad \delta v_{i_x} = \frac{\frac{e}{m_i} k_x}{\omega - k_x v_{x0}} \delta \phi. \quad (29)$$

We use Eq. (19) [or equivalently Eq. (21)] to express the complex amplitude of the potential fluctuation in terms of the density perturbation to arrive at

$$\delta \phi = \frac{k_B T_e \omega_R - \omega_0 - \omega_D + i(\omega_I + \nu_c) \frac{\delta n}{n_0}}{e \frac{\omega^* - \omega_D}{\omega^* - \omega_D}}. \quad (30)$$

Using the above equations and taking the density fluctuation to be real, without loss of generality, we arrive at the time-averaged fluctuation-induced contributions to the discharge current,

$$\langle \delta J_{e_x} \rangle = -\frac{1}{2} n_0 \frac{k_y k_B T_e \nu_c + \omega_I}{B_0} \left(\frac{\delta n_e}{n_e} \right)^2, \quad (31)$$

$$\langle \delta J_{i_x} \rangle = \frac{1}{2} e n_0 \frac{k_x}{k_{\perp}^2} (\omega_R - k_x v_{x0}) \left(\frac{\delta n_e}{n_e} \right)^2. \quad (32)$$

From these estimates, the discharge current fluctuations can be obtained. Using plausible values for our experimental conditions, i.e., $\Delta V = 23.1$ V, $n_0 = 10^{18} \text{ m}^{-3}$, $m = 3$ (decreasing voltages), $v_{x0} = -933$ m/s, and considering the density perturbations to be saturated, i.e., $\delta n/n_0 = 1$, we arrive at $\langle \delta J_{e_x} \rangle = -115.0 \text{ A/m}^2$

and $\langle \delta J_{ix} \rangle = 118.6 \text{ A/m}^2$. Taking the plasma area, $A = 7.9 \times 10^{-6} \text{ m}^2$ (using a plasma radial thickness of 0.5 mm), the corresponding currents are $\langle \delta I_{ex} \rangle = -0.903 \text{ mA}$ and $\langle \delta I_{ix} \rangle = 0.931 \text{ mA}$. The potential fluctuation that drives this current is $\delta\phi \approx 1.1 \text{ V}$. The current contributions due to electron and ion fluctuations estimated from this quasi-linear analysis are well below the current measured (typically several milliamperes) as can be seen in Figs. 6 and 7, which show that the current discharge oscillations dominate the discharge current and are consistent with the high speed camera images depicting the rotation of the plasma structures. We also note that by taking a saturated density fluctuation, we may be outside the scope of our linear analysis, in a region where the actual gradients might be steeper and thus driving a higher current. Our linear analysis, while capturing some of our experimental data, may not be adequate to describe the saturated regions, which are thought to be responsible for the measured currents. A study of the nonlinear equations will give us additional tools to model fluctuation-driven currents seen in the experiments. Such a study may also provide insight into dynamics that is seen between modes, as described in Sec. V.

V. NONLINEAR BEHAVIOR BETWEEN MODES

Here, we discuss observations that suggest dynamic behavior that cannot be described by the linear model. This seemingly nonlinear behavior is excited when transitioning between linear modes. We see this when transitioning between all of the linear modes

($m = 3, 4, 5$) observed in our experiments. The descriptor “mixed” may be somewhat of a misnomer in that the frequency contents of these “mixed” states are not a combination of the surrounding states (for example, the frequency of modes 3 and 4) but instead much more complex, consisting of higher frequencies that seem to be related through non-linear mixing. In general, it is not possible to identify a single principal frequency and a wavenumber, and the plasma does not seem to organize itself in discrete structures. Attempts to use high speed video capture of the structure during these mixed regimes reveal blurred features with little or no apparent coherence (see Fig. 13).

Figure 14 is a Fourier analysis of the temporal currents recorded through anode segments 1–3 for a discharge voltage of 257 V, placing us within an $m = 3$ and $m = 4$ mode. For this condition, we record five strong peaks, labeled $f_1 - f_5$ on a broad underlying (but much weaker) turbulent background. The frequencies are significantly higher ($>1 \text{ MHz}$) than those of the linear modes. Using a wavelet decomposition, we construct the full dispersion of these waves and the associated spectral power (Fig. 15). The frequency and wavenumbers for each peak are summarized in Table I. A close inspection of the data suggests the following relations between the modes present in this mixed regime,

$$\begin{aligned} f_3 &= f_1 + f_2, & k_3 &= k_1 + k_2, \\ f_4 &= f_5 - f_1, & k_4 &= k_5 + k_1, \\ f_5 &= f_2 + f_3, & k_5 &= k_2 + k_3. \end{aligned}$$

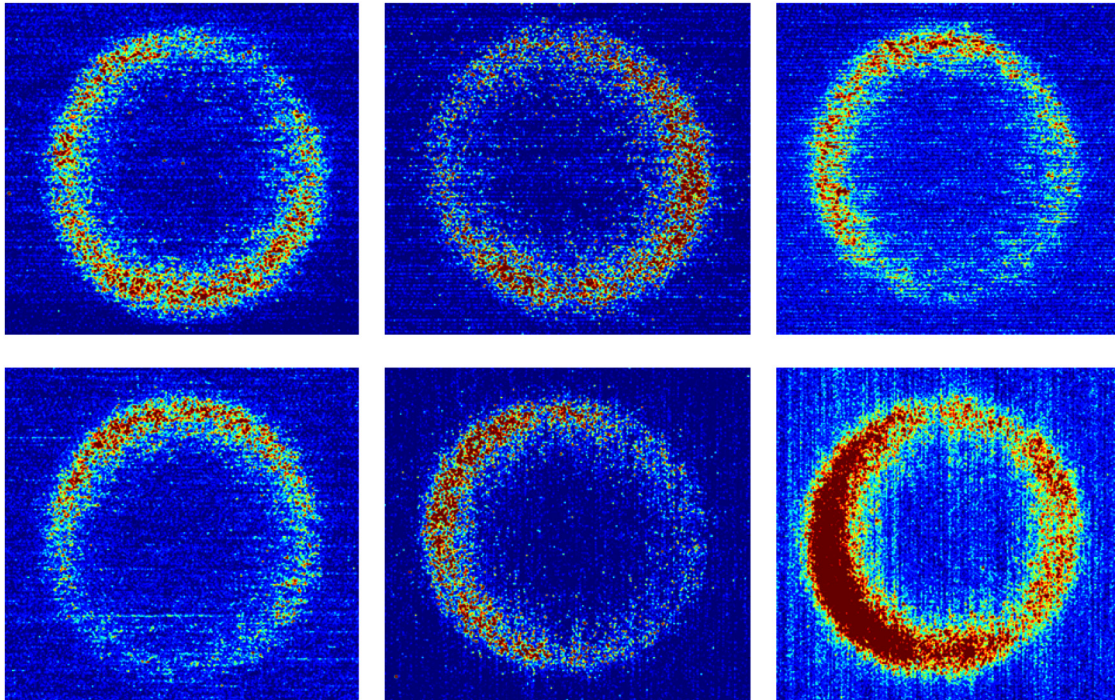


FIG. 13. High frame rate pictures of a nonlinear mode of $1 \mu\text{s}$ separation.

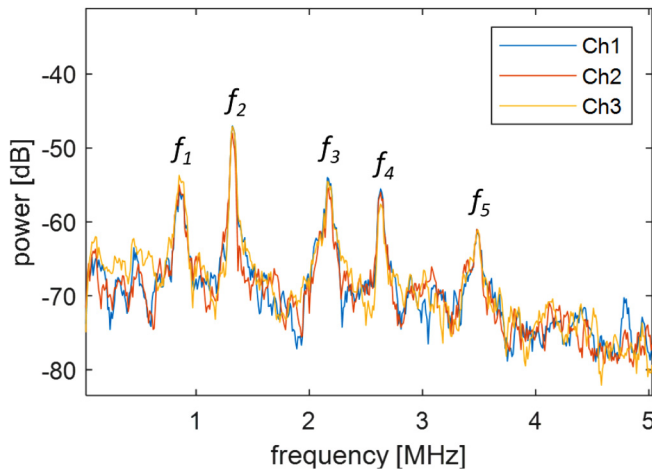


FIG. 14. Nonlinear frequency content of the current signal measured by the three segments. 5 point average filtering is applied to reduce noise (the sampling frequency is 250 MHz).

These wave energy and momentum-conserving relationships suggest the presence of three-wave mixing and the transfer of energy between one quasi-coherent state to another due to the non-linearity of the system. Such non-linear phenomenon is responsible for the transfer of energy between scales and the formation of large-scale coherent structures that may not be predicted by linear analyses. It is noteworthy that while these mixed regimes show this rich structure in the dispersion space, we do not see any discontinuity in discharge current when passing through this somewhat turbulent state of the system. A study of the nonlinear contributions to the model equations [Eqs. (11) and (13)] to better understand this mixed state of the system is the subject of future work.

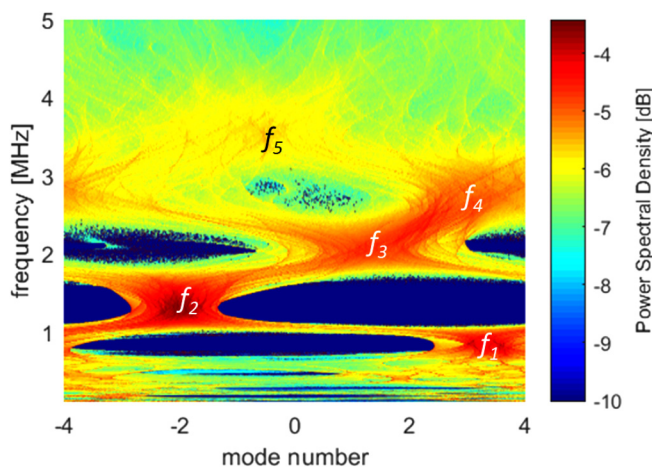


FIG. 15. Power spectrum of a nonlinear mode.

TABLE I. Location of peaks of signals in Figs. 14 and 15.

Peak	Frequency (MHz)	m (-)	k (rad/m)
f_1	0.85	3.25	230
f_2	1.31	-1.84	-130
f_3	2.16	1.41	100
f_4	2.62	2.82	200
f_5	3.47	-0.43	-30

VI. CONCLUSION AND FUTURE WORK

In this paper, we have discussed the dynamic behavior of gradient-driven drift waves in a strongly obstructed small magnetron discharge. In this particular discharge, the waves are uncharacteristically coherent, with linear growth rates generally greater than the mode frequencies of the observed rotating plasma structures. The modes and their rotation are stable over a wide range of conditions, and the rotation is retrograde to the usual externally imposed $E \times B$ direction. We have conjectured that the cause of this retrograde structure rotation is a midgap electric field reversal that is attributed to strong anode-directed electron diffusion. We have introduced a multi-fluid model for the dynamics, and a Fourier analysis of the linearized set of equations results in a dispersion relation that, with the assumption of a midgap field reversal, provides a behavior of the instabilities consistent with those seen in the experiments. Most important is that the model identifies conditions for the formation and growth of these retrograde instabilities and can describe transitions from lower to higher mode symmetries (controlled experimentally by varying the discharge voltage). Experiments are carried out with a segmented anode to confirm the localized current density. The segment currents together with high speed videography unambiguously confirm the direction of plasma rotation. An important find from the segmented anode current measurements is that there exists a stochastic regime between voltage-controlled mode transitions. An analysis of the segment currents in this regime indicates that the lower frequency state decays into a spectrum of coherent higher frequency states that exhibit features consistent with a three-wave nonlinear parametric mixing process.

It is important to emphasize that the success of this model, in its comparison with quantifiable data from the experiments, is predicated on the presence of this midgap field reversal. Such field reversals have been shown to exist in plasma sources of a similar magnetic field topology (e.g., Hall thrusters), but as of yet, we do not have direct evidence of such a reversal in our small magnetron studies. Future experiments will focus on identifying such a field reversal, perhaps through local ion velocity measurements. The success of the fluid model also speaks to the appropriateness of such a model to describe the basic dynamical features seen experimentally. As such, another future study will focus on solving the full set of equations that describe the azimuthal dynamics, including the nonlinear terms, to confirm the presence of three-wave mode-mixing, as suggested by the experiments when the discharge places the system between the lowest-order stable modes predicted by the linear analysis. Finally, two observable features that the

model predicts—a hysteresis in the mode preference depending on the continuous change in the discharge voltage and also a potentially strong dependence of the mode frequency on ion mass—will be the focus of our next experimental campaign.

ACKNOWLEDGMENTS

We wish to acknowledge the financial support of the Air Force Office of Scientific Research (AFOSR), with Dr. Mitat Birkan as Program Manager. Discussions with N. Gascon and C. Young are greatly appreciated.

DATA AVAILABILITY

The data that support the findings of this study are available within the article. Additional data, such as current traces and high resolution pictures, are available from the corresponding author upon reasonable request.

REFERENCES

- ¹A. Anders, *Surface Coatings Technol.* **257**, 308 (2014).
- ²M. Cappelli, *Phys. Today* **62**(4), 76 (2009).
- ³J. Foust, *IEEE Spectr.* **56**, 50 (2018).
- ⁴F. F. Chen, *Introduction to Plasma Physics and Controlled Fusion* (Springer, 1984). Vol. 1.
- ⁵E. Y. Choueiri, *Phys. Plasmas* **8**, 1411 (2001).
- ⁶A. Simon, *Phys. Fluids* **6**, 382 (1963).
- ⁷F. Hoh, *Phys. Fluids* **6**, 1184 (1963).
- ⁸Y. Sakawa, C. Joshi, P. Kaw, F. Chen, and V. Jain, *Phys. Fluids B: Plasma Phys.* **5**, 1681 (1993).
- ⁹A. Ehasarian, A. Hecimovic, T. De Los Arcos, R. New, V. Schulz-Von Der Gathen, M. Böke, and J. Winter, *Appl. Phys. Lett.* **100**, 114101 (2012).
- ¹⁰J. Andersson, P. Ni, and A. Anders, *Appl. Phys. Lett.* **103**, 054104 (2013).
- ¹¹A. Anders, P. Ni, and J. Andersson, *IEEE Trans. Plasma Sci.* **42**, 2578 (2014).
- ¹²A. W. Smith and M. A. Cappelli, *Phys. Plasmas* **16**, 073504 (2009).
- ¹³J. C. Perez, W. Horton, K. Gentle, W. Rowan, K. Lee, and R. B. Dahlburg, *Phys. Plasmas* **13**, 032101 (2006).
- ¹⁴T. Ito and M. A. Cappelli, *Appl. Phys. Lett.* **89**, 061501 (2006).
- ¹⁵T. Ito, N. Gascon, W. S. Crawford, and M. A. Cappelli, *J. Propul. Power* **23**, 1068 (2007).
- ¹⁶A. Kozyrev, N. Sochugov, K. Oskomov, A. Zakharov, and A. Odivanova, *Plasma Phys. Rep.* **37**, 621 (2011).
- ¹⁷A. Anders, P. Ni, and A. Rauch, *J. Appl. Phys.* **111**, 053304 (2012).
- ¹⁸T. De los Arcos, V. Layes, Y. A. Gonzalvo, V. Schulz-von der Gathen, A. Hecimovic, and J. Winter, *J. Phys. D: Appl. Phys.* **46**, 335201 (2013).
- ¹⁹Y. Yang, J. Liu, L. Liu, and A. Anders, *Appl. Phys. Lett.* **105**, 254101 (2014).
- ²⁰T. Ito, C. V. Young, and M. A. Cappelli, *Appl. Phys. Lett.* **106**, 254104 (2015).
- ²¹A. Kapulkin and M. M. Guelman, *IEEE Trans. Plasma Sci.* **36**, 2082 (2008).
- ²²W. Frias, A. I. Smolyakov, I. D. Kaganovich, and Y. Raitses, *Phys. Plasmas* **19**, 072112 (2012).
- ²³M. K. Scharfe, N. Gascon, M. A. Cappelli, and E. Fernandez, *Phys. Plasmas* **13**, 083505 (2006).
- ²⁴F. Parra, E. Ahedo, J. Fife, and M. Martinez-Sanchez, *J. Appl. Phys.* **100**, 023304 (2006).
- ²⁵A. Anders, *Appl. Phys. Lett.* **105**, 244104 (2014).
- ²⁶N. Brenning, C. Huo, D. Lundin, M. Raadu, C. Vitelaru, G. Stancu, T. Minea, and U. Helmersson, *Plasma Sources Sci. Technol.* **21**, 025005 (2012).
- ²⁷D. Meeker, see <http://www.femm.info/wiki/HomePage> for “Finite Element Method Magnetism” (2011).
- ²⁸N. B. Meezan, W. A. Hargus, Jr., and M. A. Cappelli, *Phys. Rev. E* **63**, 026410 (2001).
- ²⁹V. Morin and A. I. Smolyakov, *Phys. Plasmas* **25**, 084505 (2018).
- ³⁰A. Smolyakov, O. Chapurin, W. Frias, O. Koshkarov, I. Romadanov, T. Tang, M. Umansky, Y. Raitses, I. Kaganovich, and V. Lakhin, *Plasma Phys. Control. Fusion* **59**, 014041 (2016).